

Supporting Information for the Manuscript:

Photoinduced Electron Injection in a Fully
Solvated Dye-Sensitized Photoanode:

A Dynamical Semi-Empirical Study

Jan Paul Menzel†, Anastasios Papadopoulos†•, Jelena Belić‡, Huub de Groot†, Lucas
Visscher‡, Francesco Buda†**

† Leiden Institute of Chemistry, Leiden University, PO Box 9502, 2300 RA Leiden, The
Netherlands.

• Present address: Department of Molecular Theory and Spectroscopy, Max-Planck-Institut
für Kohlenforschung, Kaiser-Wilhelm-Platz 1, 45470 Mülheim and der Ruhr, Germany.

‡ Department of Chemistry and Pharmaceutical Sciences, Vrije Uversiteit Amsterdam, De
Boelelaan 1083, Amsterdam 1081 HV, The Netherlands.

Corresponding Author

*E-mail: f.buda@chem.leidenuniv.nl, j.p.menzel@lic.leidenuniv.nl

SI-1 Construction of the dye-sensitized photoanode

SI-2 Real time simulation of photoinduced electron injection

SI-3 Extended Hückel parameter optimization

SI-4 Influence of dihedral angle on electron injection

SI-5 Resonance coupling in the electron transfer process

SI-6 Photoinduced electron injection – Catechol

SI-7 Photoinduced electron injection – Benzoic acid

SI-8 Photoinduced electron injection – Benzohydroxamic acid

SI-9 Photoinduced electron injection – Cat-NDI

SI-10 Photoinduced electron injection – Ben-NDI

SI-11 Photoinduced electron injection – Hyd-NDI

SI-1 Construction of the dye-sensitized photoanode system

The Photoanode system is modelled with SCC-DFTB¹⁻³ using the DFTB program included in the Amsterdam Density Functional Modeling suite.^{4,5} The tiorg-0-1 parameter set was chosen.⁶ To model the TiO₂ anatase electrode, first a bulk optimization was performed using a supercell of 48 atoms in total (16 titanium atoms, 32 oxygen atoms) and periodic boundary conditions. The box size was optimized as well. The resulting geometry can be seen in Figure S1.

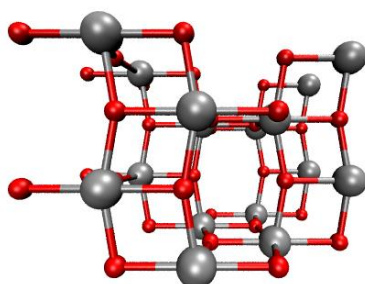


Figure S1. Optimized geometry of bulk anatase. Only one supercell is shown.

The result was used to construct the anatase (101) surface, with the surface normal along z, including 144 atoms and three layers. The lowest layer was kept frozen during optimization to maintain bulk geometry, while the upper two layers were reoptimized to allow for surface relaxation effects. The corresponding box size was 10.045 Å x 15.234 Å x 70.000 Å. Anchoring molecules were attached via bidentate bridging mode, with the dissociating protons adsorbed on the surface as seen in Figure S2.

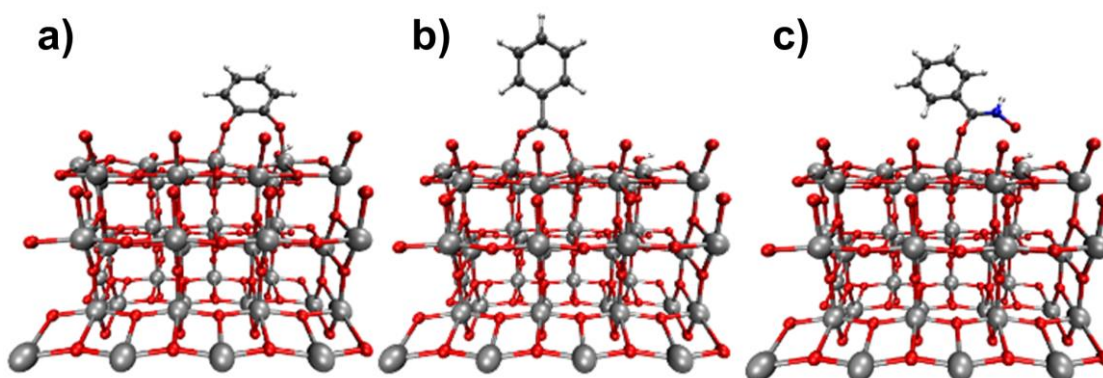


Figure S2. Optimized geometry of catechol (a), benzoic acid (b) and benzohydroxamic acid (c) on anatase (101) surface.

To simulate the electrolyte environment, water molecules were added to the box in such a way, that the density of the box above the anatase surface corresponded to about 1g/ml. Several water molecules were frozen far above the surface (20 Å) to keep the water molecules from diffusing into vacuum.

These water layers were constructed using a configuration extracted from bulk water equilibrated at 300K. For equilibration purposes, 5 ps long trajectories using SCC-DFTB/tiorg-0-1 were generated in the NVT ensemble with a 1 fs time step using a Berendsen thermostat⁷ at 300 K. For the electron injection simulations, a total of 1.5 ps with a time step of 0.1 fs in the NVE ensemble was then generated, starting with geometries and velocities from the NVT results. These trajectories were then cut in 15 single trajectories each consisting of 1000 steps with a total length of 100 fs. Those were used for the Extended Hückel based quantum dynamics of the photoexcited electron and hole. For the simulations of the core extended NDI dyes, the same general procedure was followed. A simulation box of 20.091 Å x 22.851 Å x 150.000 Å was used containing 3 layers of anatase with the (101) surface normal in z direction. The lowest layer was kept frozen at bulk geometry. The core extended NDIs were attached via their linking groups in the bidentate bridging mode; the protons dissociated from the linking group were adsorbed on the surface. The box was filled with water molecules to obtain a density of 1g/ml, with a layer of water molecules frozen at a distance of about 20 Å. NVT runs of 5 ps using a Berendsen thermostat at 300 K were used for equilibration, using a 1 fs time step. This was followed by NVE runs for a length of 2.5 ps using a time step of 0.1 fs. These trajectories were divided into 5 slices each of 500 fs to be used in the time propagation of photoexcited electron and hole.

SI-2 Real time simulations of photoinduced electron injection

The photoinduced electron injection from a dye molecule into the TiO₂ electrode are simulated in real time via a quantum-classical semiempirical approach. Nuclear trajectories in the ground state are generated *a priori* using molecular dynamics based on the semi empirical Self Consistent Charge – Density Functional based Tight Binding (SCC-DFTB)^{1–3} method. These nuclear trajectories, as well as their starting geometries are then used for the quantum propagation of the photoexcited electron and hole. These Electron Transfer Dynamics (ETD) are based on an Extended Hückel based tight binding Hamiltonian and propagated in time with the AO/MO time propagator.⁸ To represent an excitation of the dye, the initial wave packets for photoexcited electron and hole were chosen as the Highest Occupied Molecular Orbital (HOMO) and Lowest Unoccupied Molecular Orbital (LUMO) of the dye molecule. These orbitals are fragment orbitals constructed with only the Atomic Orbitals (AOs) of the atoms included in the corresponding adsorbed dye molecule. The wave packet $\Psi(t)$ is then projected onto the adiabatic Molecular Orbitals (MOs) φ of the entire system constructed by diagonalization of the total Hamiltonian:

$$|\Psi(t)\rangle = \sum_{\varphi} C_{\varphi}(t) |\varphi\rangle.$$

The molecular orbital coefficients C_{φ} are propagated in time according to the following equation

$$C_{\varphi}(\delta t) = C_{\varphi}(0) e^{\frac{-iE_{\varphi}\delta t}{\hbar}}$$

where E_{φ} are the molecular orbital eigenvalues. The MOs as well as the Hamiltonian are thereby assumed to be time independent within the time slice δt . After propagation, the wave packet is projected back onto the AO basis. The AOs are then shifted according to the new nuclear positions, the new Hamiltonian is diagonalized and new MOs are obtained. The wave packet is then projected onto this new MO basis. This projection between adiabatic (MO) and diabatic (AO) basis allows for transition between adiabatic states. Through the changes in the nuclear positions, the Hamiltonian shows indirect time dependence between time slices. A more in depth description of the method can be found in references^{8,9}. We chose the same time step of 0.1 fs for nuclear and electronic propagation. This small time step is necessary for a stable simulation where the time independence of the Hamiltonian during a nuclear time step is a reasonable approximation. The propagation is done for a total of 100 fs (anchoring molecules) or 500 fs (core extended NDIs).

SI-3 Extended Hückel parameter optimization

In the quantum dynamics calculations, the correct energetic values of the involved orbitals are crucial, since they determine the thermodynamic driving force as well as the time evolution of the electronic wave packets. They are obtained using a tight binding Hamiltonian based on Extended Hückel theory that is described elsewhere⁹. To obtain reliable results, we need to optimize the semi-empirical parameters defining the matrix elements of the Extended Hückel Hamiltonian in such a way that they reproduce experimental values. As there is only limited experimental information on some of the investigated molecules, an alternative to experimental values is needed for parameter optimization. Here, we use $\Delta\text{SCF}^{10,11}$ values obtained in implicit solvation to obtain the ionization potential that is related to the HOMO via the Koopmans theorem.¹² Thereby, a geometry optimization of the neutral species was performed, as well as an unrestricted calculation on this same geometry with one electron removed. The energy difference between these two SCF calculations is then a reasonable estimate of the experimental oxidation potential. These values were calculated with the ADF program by SCM^{4,13} on the DFT/B3LYP^{14–16} level using a DZP basis set¹⁷ and D3 dispersion corrections with BJ-damping^{18,19} within COSMO²⁰ implicit water solvation. This combination was chosen, since the ΔSCF results in the corresponding implicit solvation agree reasonably well with available experimental oxidation potentials (see Table S1).

Table S1: Experimental oxidation potential, ΔSCF estimate using B3LYP/DZP, D3 with BJ-damping and COSMO solvation of the solvent used in the experiment and COSMO water.

Molecule	Solvent used in experiment	ΔSCF in experimental solvent [eV]	Experimental Oxidation Potential [V]		ΔSCF in COSMO water [eV]
Catechol	Acetonitrile	-5.86	-5.83 ²¹		-5.79
Benzoic acid	Water	-7.07	-		-7.07
Benzhydroxamic acid	Water	-6.74	-		-6.74
NDI	Dichloromethane (DCM)	-7.01	-7.07 ²²		-6.94
NDI_2OEt	DCM	-6.31	-6.16 ²²		-6.05
NDI_2NHEt	DCM	-5.45	-5.35 ²²		-5.20
NDI_NHEt_OEt	DCM	-5.81	-5.75 ²²		-5.55

For the NDI based dyes, the LUMO target energy was obtained by using the before mentioned ΔSCF value for the HOMO energy and adding the TD-DFT HOMO-LUMO excitation energy obtained on the same geometry with the same settings. These values agree reasonably well with experimental values for several tested NDIs (see Table S2). Recently, also Narsaria *et al.* showed that B3LYP excitation energies for NDIs have a strong correlation with experimental excitation energies.²³

Table S2: Experimental oxidation potential, Δ SCF estimate using B3LYP/DZP, D3 with BJ-damping and COSMO solvation of the solvent used in the experiment, Δ SCF + TDDFT excitation energy estimate, experimental reduction potential. Values differing more than 0.2 eV marked in bold.

Molecule	Solvent used in experiment	Δ SCF in experimental solvent [eV]	Experimental Oxidation Potential [V]	Δ SCF + TDDFT Excitation energy (in brackets)	Experimental Reduction Potential
Catechol	Acetonitrile	-5.86	-5.83 ²¹	-0.93 (4.93)	-1.65²¹
NDI	DCM	-7.01	-7.07 ²²	-3.91 (3.10)	-4.01 ²²
NDI_2OEt	DCM	-6.31	-6.16 ²²	-3.77 (2.55)	-3.82 ²²
NDI_2NHet	DCM	-5.45	-5.35 ²²	-3.52 (1.94)	-3.56 ²²
NDI_NHet_OEt	DCM	-5.81	-5.75 ²²	-3.62 (2.20)	-3.75 ²²

Unfortunately, for the benzene based anchoring groups, this method does not give an accurate estimate and thus a different approach has been taken. The Δ SCF value still describes the experimental oxidation potential reasonably well and therefore is still taken as a reference for the HOMO energy. For the LUMO energy, the Δ SCF value plus the experimental onset of the first UV-Vis absorption peak is taken as reference, since also in experiments, difficult redox potentials are often estimated using this onset value and subtracting / adding it to the more easily obtained redox potential (reduction / oxidation potential).^{21,22}

To summarize, the target energies for the frontier orbitals are obtained as follows: For all molecules, the Δ SCF values in water (COSMO) were used as HOMO target value. For the anchoring molecules catechol, benzoic acid and benzohydroxamic acid, the experimental first absorption peak onset energy was added to the Δ SCF value to obtain an estimate for the LUMO energy. For the NDI-derived molecules, the TDDFT excitation energies in COSMO using B3LYP/DZP for the excitation with the largest oscillator strength (here always the HOMO-LUMO excitation) were added to the Δ SCF values as an estimate for the LUMO energy. The values are reported in Table S3.

Table S3: Target energies for HOMO (Δ SCF) and LUMO (either Δ SCF + TDDFT excitation energy or Δ SCF + experimental absorption peak onset energy).

Molecule	Target HOMO [eV]	Target LUMO [eV]	
		Δ SCF + TDDFT excitation energy in water (brackets)	Δ SCF + experimental absorption peak onset (brackets)
Catechol	-5.79		-1.61 (4.18 ²¹)
Benzoic Acid	-7.07		-2.77 (~4.3 ²⁴)
Benzohydroxamic Acid	-6.74		-2.44 (~4.3 ²⁴)
2OEt-NDI	-6.05	-3.56 (2.50)	
Cat-NDI	-5.55	-3.50 (2.05)	
Ben-NDI	-6.06	-3.88 (2.18)	
Hyd-NDI	-6.04	-3.88 (2.16)	

Optimization of the parameters was performed on the free dye and anchor molecules: they were optimized in their neutral (thus protonated) form before dissociative adsorption on the TiO₂ surface. Since the nuclear dynamics were performed using SCC-DFTB¹⁻³ with the tiorg-0-1 parameter set⁶, the geometry optimization was performed with the same settings.

Since the conduction band edge of the TiO₂ with the Extended Hückel Hamiltonian is at -10.00 eV and the experimental value for the anatase conduction band edge is at approximately -4.05 eV²⁵, the target values of the frontier orbitals of the molecules are shifted by -5.95 eV to give the correct energetic alignment. The optimization procedure itself was performed using a genetic algorithm and cost function that are described elsewhere.⁹ Only HOMO and LUMO energies were used as targets. In Table S4 we compare the HOMO and LUMO energies obtained with standard parameters, the target values and the energies obtained with the optimized parameters.

Table S4: HOMO/LUMO energies for the different molecules obtained with standard Hückel parameters, target values generated above with linear shift of -5.95 eV and obtained with optimized Hückel parameters.

Molecule	Standard Hückel Parameters [eV]		Target values [eV]		Optimized Hückel parameters [eV]	
	HOMO	LUMO	HOMO	LUMO	HOMO	LUMO
Catechol	-12.20	-8.17	-11.74	-7.56	-11.75	-7.55
Benzoic Acid	-12.81	-9.62	-13.02	-8.72	-13.02	-8.72
Benzohydroxamic Acid	-12.69	-9.43	-12.69	-8.39	-12.70	-8.39
2OEt-NDI	-12.14	-10.63	-12.00	-9.51	-12.00	-9.52
Cat-NDI	-11.96	-10.76	-11.50	-9.45	-11.50	-9.45
Ben-NDI	-12.10	-10.84	-12.01	-9.83	-12.01	-9.83
Hyd-NDI	-12.07	-10.83	-11.99	-9.83	-11.96	-9.81

The spatial distribution of the frontier orbitals was checked against their respective B3LYP counterparts to exclude unphysical orbitals. For the anchoring molecules, this was extended to HOMO-1 and LUMO+1 as well, since their high symmetry results in several near degenerate states that might mix and cross due to changing nuclear geometries. In Tables S5 and S6, the spatial distribution of the frontier orbitals using B3LYP/COSMO and Extended Hückel using the optimized parameters are shown for the anchoring molecules and dyes. The optimized parameters give frontier orbital energies as well as spatial distributions that are very close to the B3LYP results.

Table S5: Spatial distribution of HOMO-1, HOMO, LUMO and LUMO+1 for the three anchoring molecules, using B3LYP and the Extended Hückel method with optimized parameters

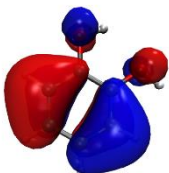
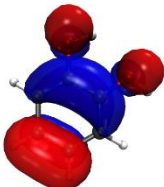
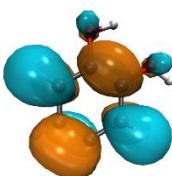
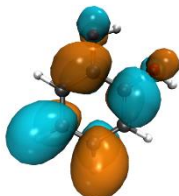
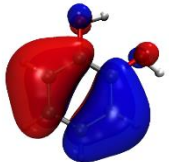
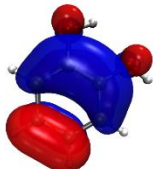
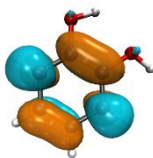
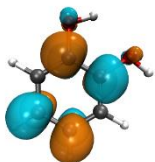
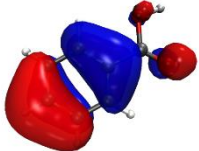
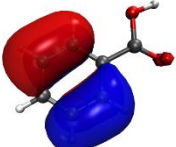
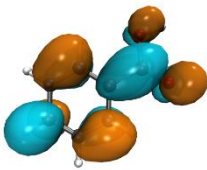
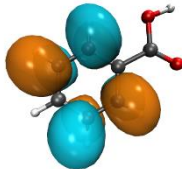

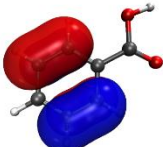
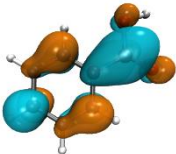
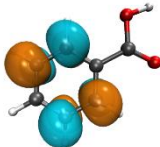

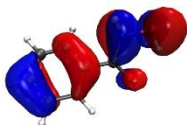
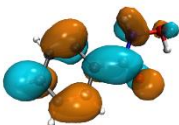
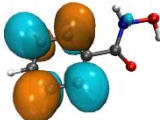
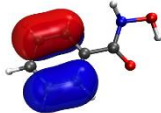
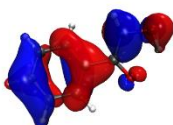
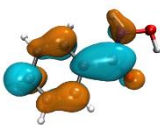
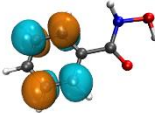
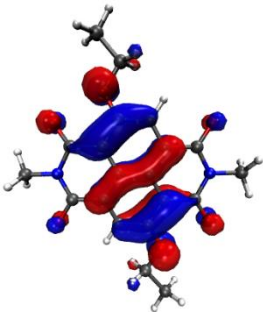
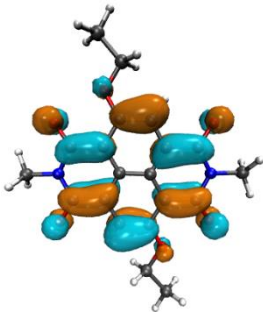
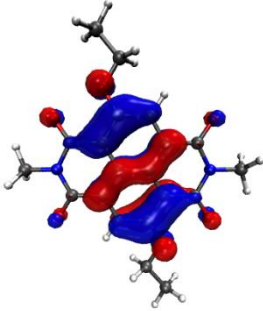
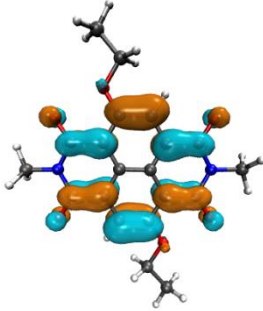
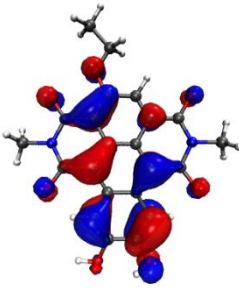
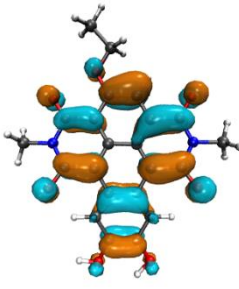
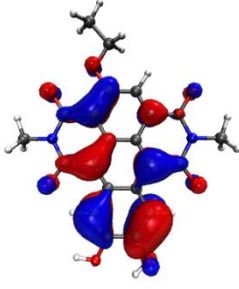
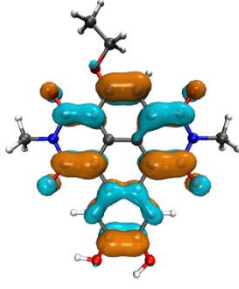
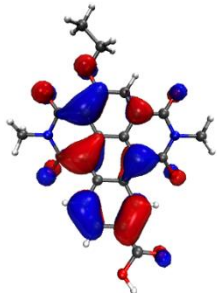
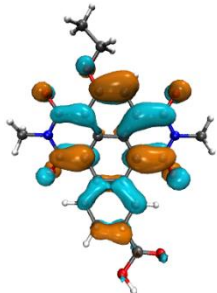
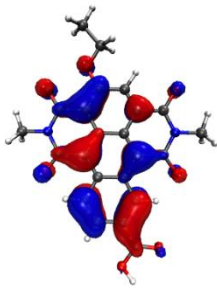
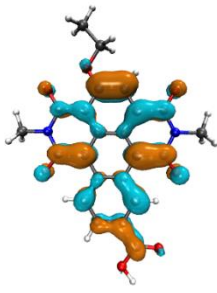
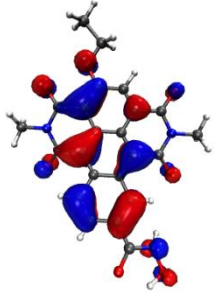
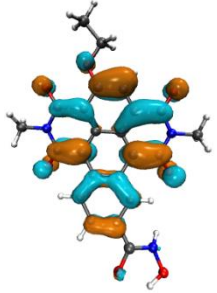
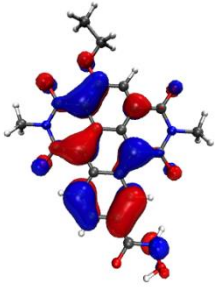
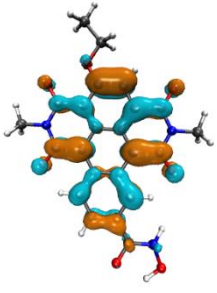
Molecule /Method	HOMO-1	HOMO	LUMO	LUMO+1
Catechol				
B3LYP				
Extended Hückel Optimized				
Benzoic Acid				
B3LYP				
Extended Hückel Optimized				
Benzohydroxamic Acid				
B3LYP				
Extended Hückel Optimized				

Table S6: Spatial distribution of HOMO and LUMO for the NDI-based dyes, using B3LYP and the Extended Hückel method with optimized parameters

Molecule / Method	HOMO	LUMO
2OEt-NDI		
B3LYP		
Extended Hückel Optimized		
Cat-NDI		
B3LYP		
Extended Hückel Optimized		

Ben-NDI		
B3LYP		
Extended Hückel Optimized		
Hyd-NDI		
B3LYP		
Extended Hückel Optimized		

In Figure S3, the energetic alignment of the frontier orbitals of all optimized molecules are shown in comparison to the TiO₂ conduction band edge. As can be seen, all molecules have sufficient driving force to inject into the conduction band. The benzene derived anchoring groups have significantly higher LUMO energies than the NDI derived dyes. The carboxylic acid and hydroxamic acid-based core extended ethoxy NDIs have very similar LUMO energies close to the conduction band edge, while the catechol increases both the HOMO and LUMO energy values of the NDI in comparison to the other two anchoring groups.

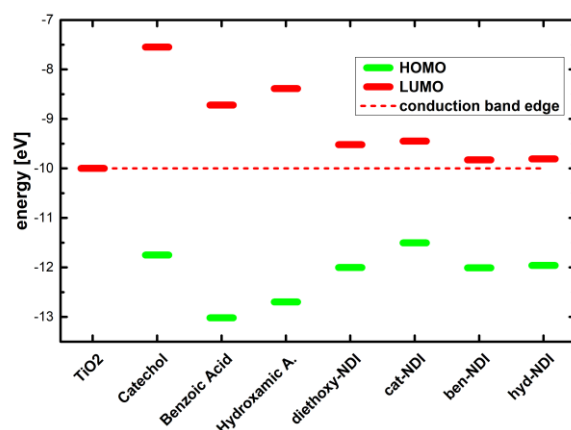


Figure S3. HOMO and LUMO energies of the investigated anchoring molecules and dyes in comparison to the conduction band edge of anatase (dashed line) obtained with the Extended Hückel method using the optimized parameters

Of course, this alignment might change during the attachment of the molecules on the TiO₂ surface and also during the dynamics. In Figure S4, the Partial Density of States (PDOS) of TiO₂ and the investigated anchoring molecules from the full photoanode system, with anchoring molecules attached to the electrode and explicit solvent is shown for comparison.

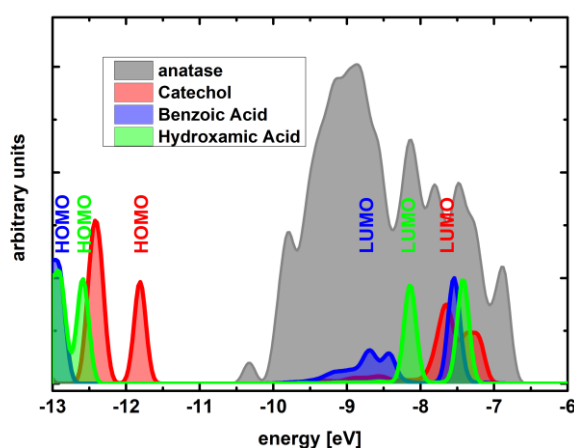


Figure S4. Partial Densities of States (PDOS) in band gap and conduction band of the TiO₂ electrode (grey) and the adsorbed anchoring molecules catechol (red), benzoic acid (blue) and benzohydroxamic acid (green). The TiO₂ PDOS has been divided by 5 for easier comparison. Frontier orbitals are marked.

All three anchoring molecules have a LUMO energy that is well within the conduction band of the TiO₂. Therefore, there is a driving force to inject a photoexcited electron into the conduction band. Catechol has the highest LUMO, followed by the benzohydroxamic acid and then the benzoic acid.

The benzoic acid has a low amount of state density below the LUMO that comes from conduction band states that extend over the carboxylic acids' oxygens. This overlap might also explain the initial ultrafast injection of the benzoic acid, where the electron wave packet rapidly expands from the fragment LUMO onto states involving the TiO_2 . In general, the HOMO – LUMO gap of the anchoring molecules is quite high and the LUMO well above the conduction band edge.

In Figure S5, the PDOS of the core extended ethoxy NDI molecules is shown in comparison to the TiO_2 .

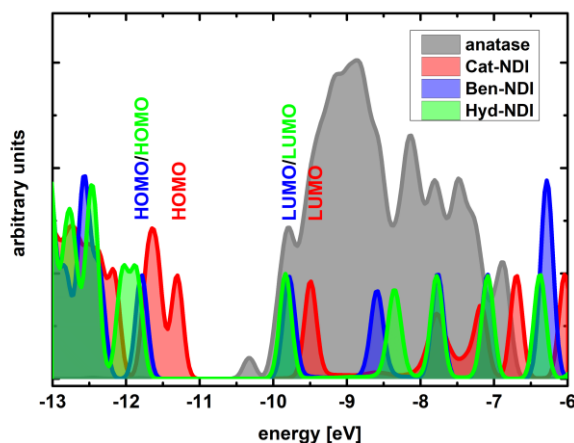


Figure S5. Partial Densities of States (PDOS) in band gap and conduction band of the TiO_2 electrode (grey) and the adsorbed anchoring molecules cat-NDI (red), ben-NDI (blue) and hyd-NDI (green).

The TiO_2 PDOS has been divided by 5 for easier comparison. Frontier orbitals are marked.

HOMO-LUMO gaps are significantly lower than for the respective anchoring molecules. Cat-NDI has the highest LUMO energy, above the conduction band edge. Ben-NDI and Hyd-NDI show very similar PDOS, with their LUMOs slightly above the conduction band edge. Here, the driving force is significantly lower than for the anchoring molecules, which is reflected in their significantly lower injection rates. However, the HOMO-LUMO gap lies for all three NDI molecules well in the visible light range and alignment seems favorable.

SI-4 Influence of dihedral angle on electron injection

In some of the ETD simulations, the observed delay in the injection can be tightly associated to the dihedral angle between the anchoring group and the aromatic system of the organic molecule. One such example is shown in Figure S6, where electron injection from benzohydroxamic acid is shown. A simulation with delayed injection was chosen and compared to the associated change in dihedral angle shown in the inset chemical structure. Injection is hindered when the angle approaches 90 degrees, breaking possible conjugation between the benzene group and the hydroxamate subsystem.

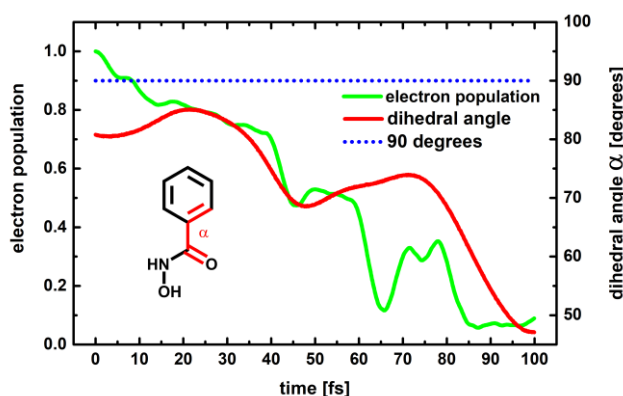


Figure S6. Electron population on ben-NDI over time (green) in comparison to dihedral angle α (red) shown in the inlet structure. The dotted blue line corresponds to 90 degrees. Electron injection is hindered when the dihedral angle is close to 90 degrees, breaking conjugation.

In Figure S7, an example is given from the ben-NDI case. The initial electron injection is fast, but at around 150 fs is stagnating, while the dihedral angle approaches 90 degrees with the aromatic system and anchoring group perpendicular to each other. For about 250 fs, the injection process is halted and only starts again when the dihedral angle leaves the region around 90 degrees, opening a channel via the anchoring group.

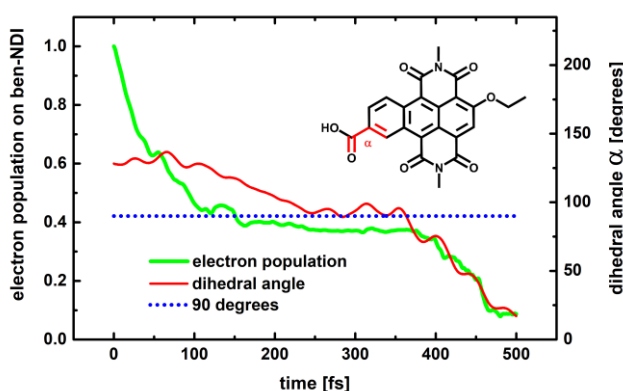


Figure S7. Electron population on ben-NDI over time (green) in comparison to dihedral angle (red) shown in the inlet structure. The dotted blue line corresponds to 90 degrees. Electron injection is hindered when the dihedral angle is close to 90 degrees, breaking conjugation.

SI-5 Resonance coupling in the electron transfer process

As shown before, the nuclear geometries can allow or prohibit electron flow from the photoexcited dye towards the electrode. However, the nuclear motion itself can also be used by the electron for a rapid injection by taking advantage of resonant coupling. Whereas the electronic system is not able to activate nuclear modes and slow down the nuclear motion in the sense of coherent conversion from reactant to product state, it can use present modes available through the incoherent thermal noise for a nonadiabatic population transfer. As the LUMO of the dye molecules lays energetically within the conduction band of the TiO_2 electrode, the energy difference between electronic states is very small and a myriad of different states can couple to another. This leads to a very rich selection of modes that the electronic system can couple to in the region below 1000 cm^{-1} . Both, the electronic frequencies as well as the total nuclear vibrational density of states (VDOS) of a single electron injection trajectory of the photoexcited hydNDI molecule, are given in Figure S8. Water molecules are omitted from the VDOS for clarity. As is clear from the figure, most electronic frequencies (red) lie in the region below 1000 cm^{-1} , where a large variety of nuclear modes (blue) is available. Over the course of the injection process, the electronic system can therefore couple to several nuclear modes, with some modes becoming more pronounced over the trajectory and others whose role diminishes. We note that this huge variety of possible pathways also leads to a significant speed-up of the conversion, especially within the electrode, since the high density of electronic states in the conduction band lead to a quick conversion to low lying states. In this system, the role of resonant coupling plays therefore an important role, but which exact modes couple to this process is of less relevance since there is a wide collection of modes available, that have very similar frequencies: there will always be a mode of correct frequency available.

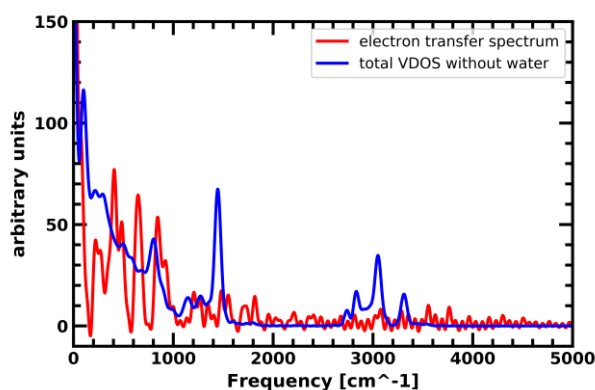


Figure S8. Electron transfer frequencies (red) and total VDOS (blue) of a single trajectory of electron injection from photoexcited hydNDI with explicit water. The water molecules are removed from the VDOS for clarity. Notable are the large peaks in the electron transfer frequencies at low wavenumbers and the abundance of nuclear modes in the same region. A gaussian window function with a sigma value of 5 was used to reduce noise.

Nevertheless, we show an example of resonant coupling between the electronic system and a specific nuclear mode below in figure S9, that becomes so dominant in a part of the trajectory, that it can clearly be associated to the conversion process. The electronic frequencies and VDOS of the dihedral angle shown in the inset are given for the time 150-250 fs, where the coupling is most pronounced.

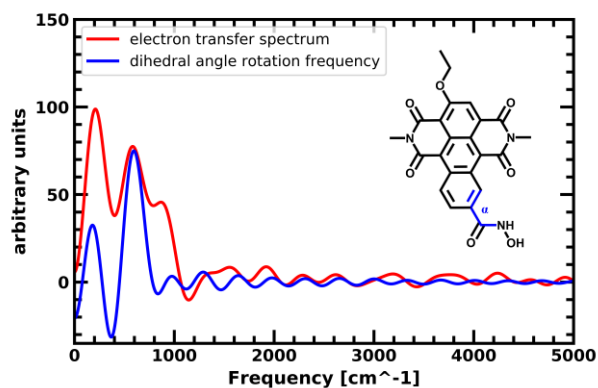


Figure S9. Electron transfer frequency (red) and frequencies of the dihedral angle rotation (blue) marked in the inset for the same trajectory as above between 150 and 250 fs. There is a clear resonance between the nuclear mode and the electron transfer frequencies with a peak at around 570 cm^{-1} . A gaussian window function with a sigma of 1 was used to reduce noise.

For a more detailed view on resonant coupling and coherent charge transfer, see e.g. reference ²⁶.

SI-6 Photoinduced electron injection – Catechol

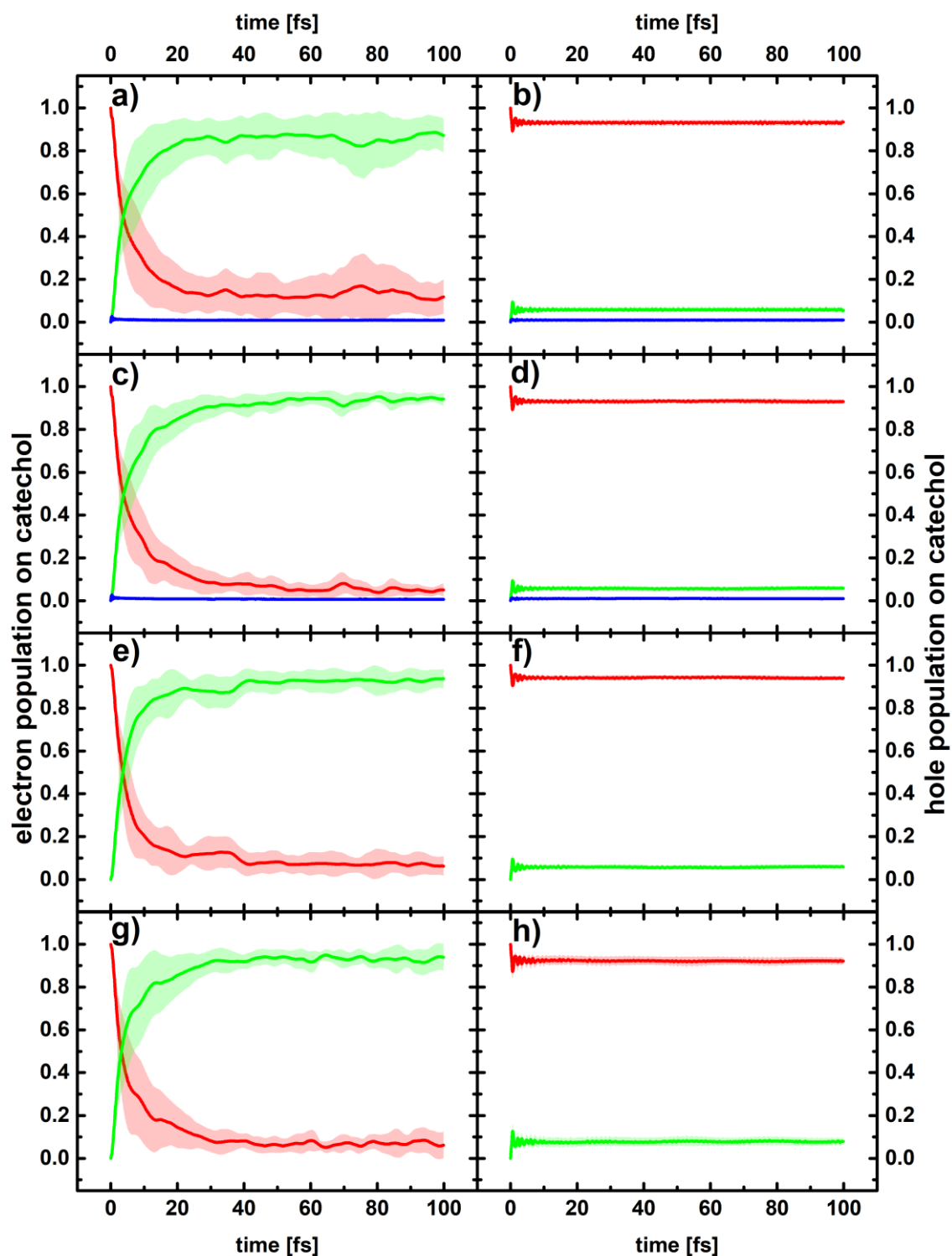


Figure S10. Electron population (left panels) and hole population (right panels) on catechol (red), TiO_2 (green) and water (blue) averaged over 15 ETDs on **a)/b)** static geometries, **c)/d)** nuclear trajectories with explicit solvation, **e)/f)** nuclear trajectories with explicit water removed, **g)/h)** nuclear trajectories without water. The bold lines denote the mean value, the shaded areas represent the standard deviation centered on the mean value.

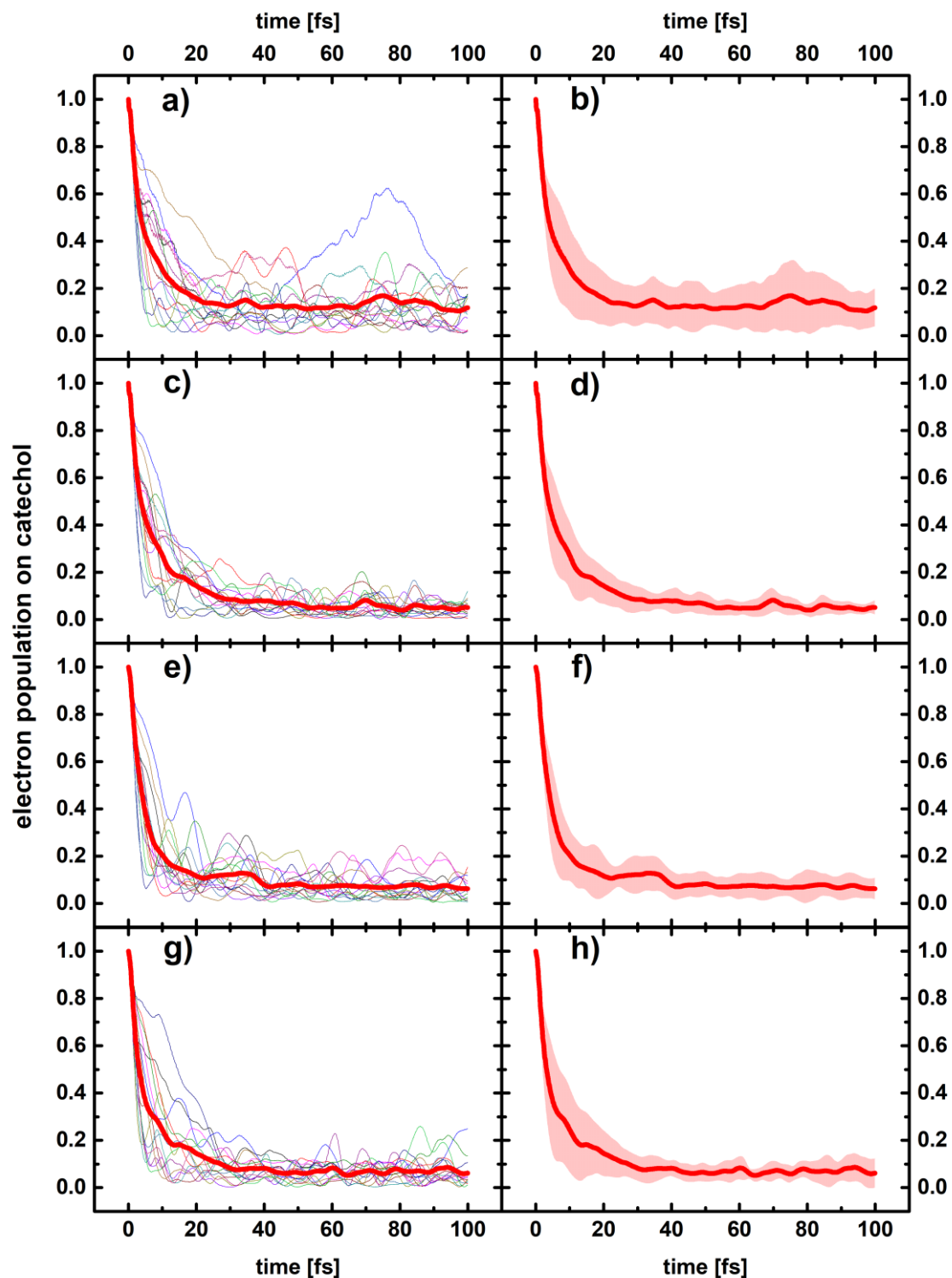


Figure S11. Electron population on catechol. The left panels show the 15 single ETD runs in narrow lines, the resulting mean average in bold red; the right panels give this same mean average in bold red with the shaded areas representing the standard deviation. Results obtained on **a/b)** static geometries, **c/d)** nuclear trajectories with explicit water, **e/f)** nuclear trajectories with water removed, **g/h)** nuclear trajectories without water.

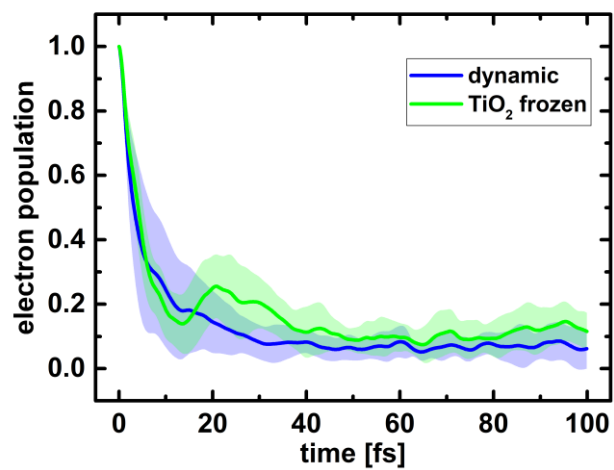


Figure S12. Electron population on catechol averaged over 15 ETDs without explicit solvation allowing for TiO₂ nuclear dynamics (blue) and when freezing the TiO₂ electrode (green). The bold lines represent the mean value, the shaded areas the standard deviation.

SI-7 Photoinduced electron injection – Benzoic acid

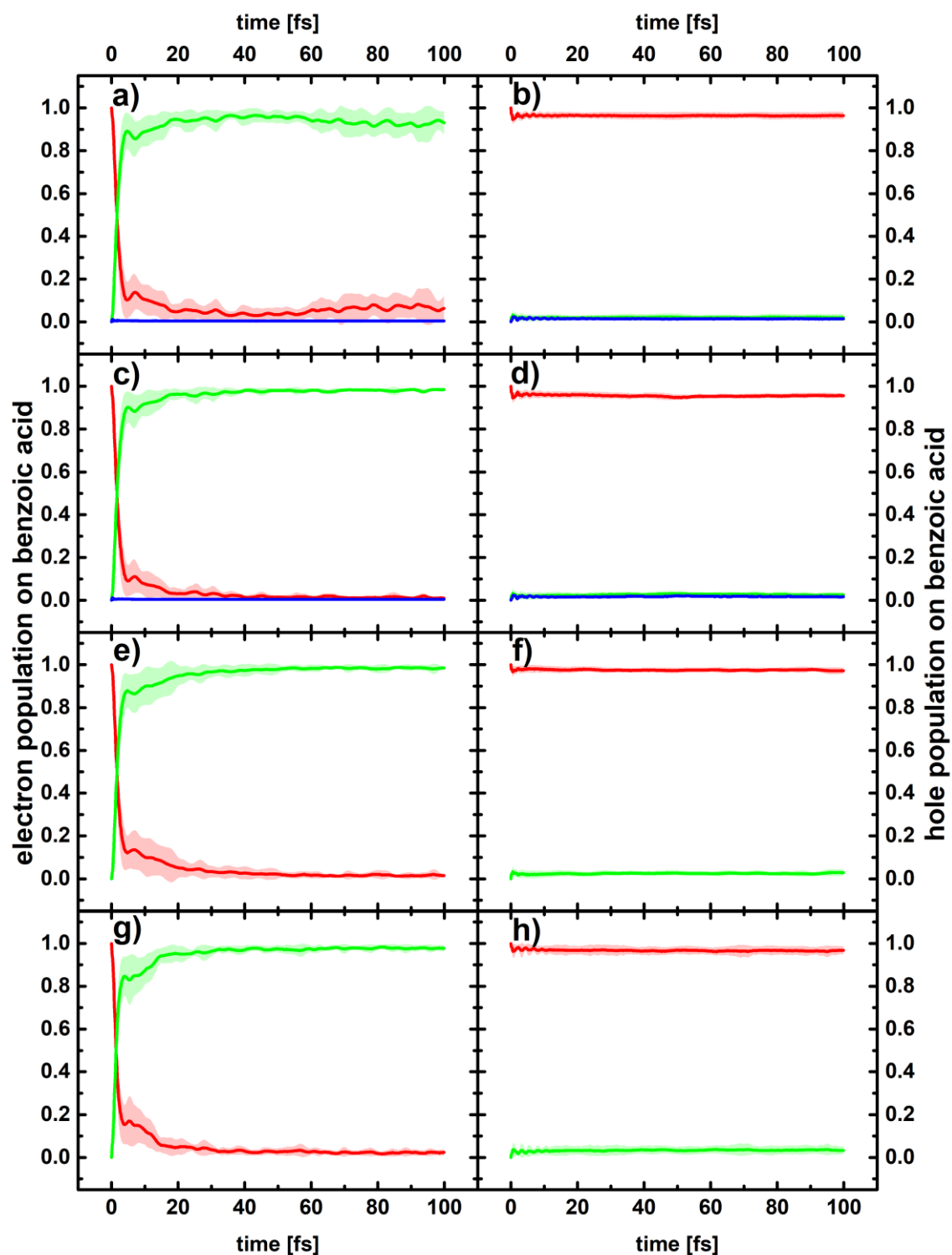


Figure S13. Electron population (left panels) and hole population (right panels) on benzoic acid (red), TiO₂ (green) and water (blue) averaged over 15 ETDs on **a)/b)** static geometries, **c)/d)** nuclear trajectories with explicit solvation, **e)/f)** nuclear trajectories with explicit water removed, **g)/h)** nuclear trajectories without water. The bold lines denote the mean value, the shaded areas represent the standard deviation centered on the mean value.

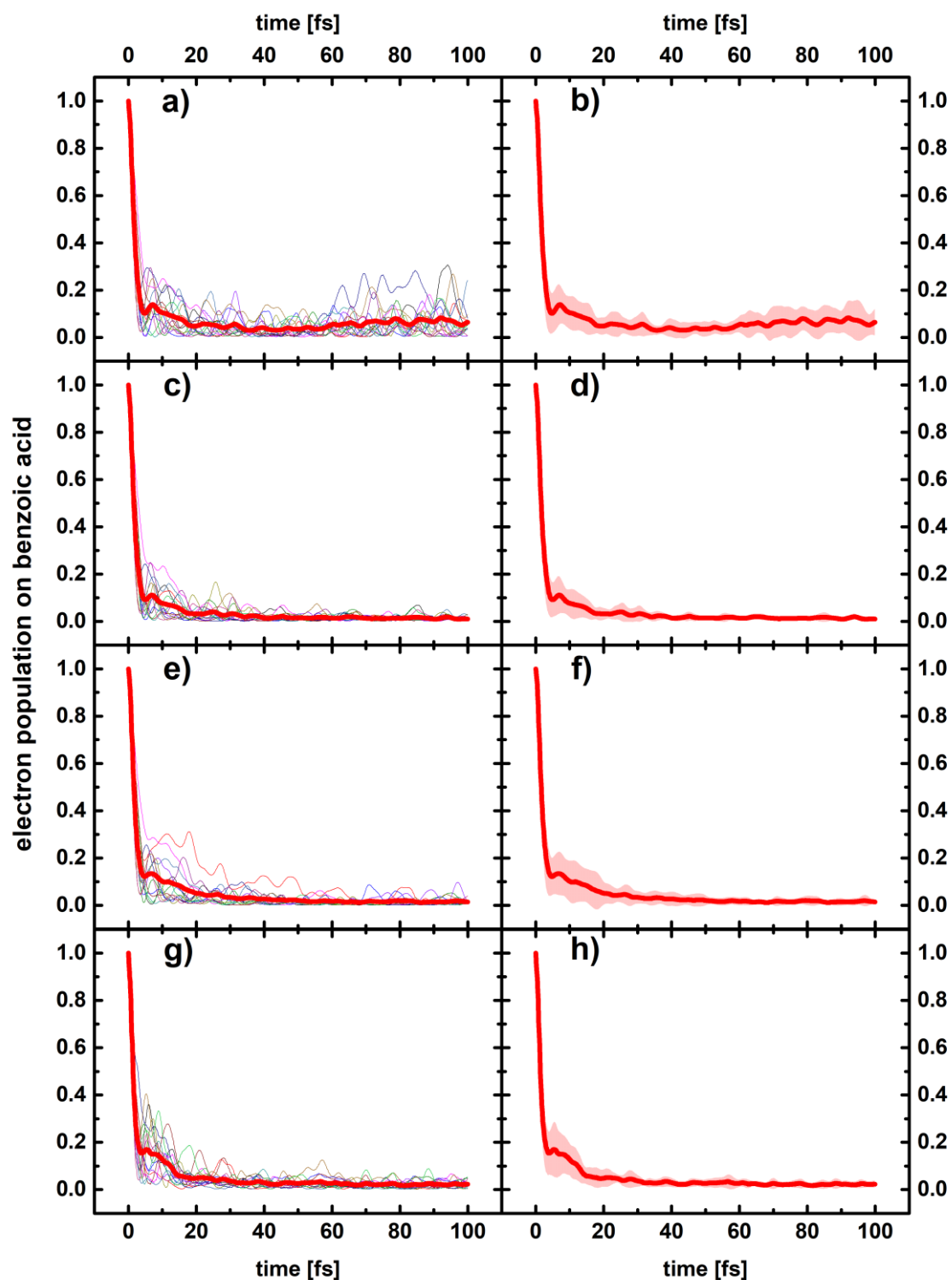


Figure S14. Electron population on benzoic acid. The left panels show the 15 single ETD runs in narrow lines, the resulting mean average in bold red, the right panels give this same mean average in bold red with the shaded areas representing the standard deviation. Results obtained on **a/b)** static geometries, **c/d)** nuclear trajectories with explicit water, **e/f)** nuclear trajectories with water removed, **g/h)** nuclear trajectories without water.

SI-8 Photoinduced electron injection – Benzohydroxamic acid

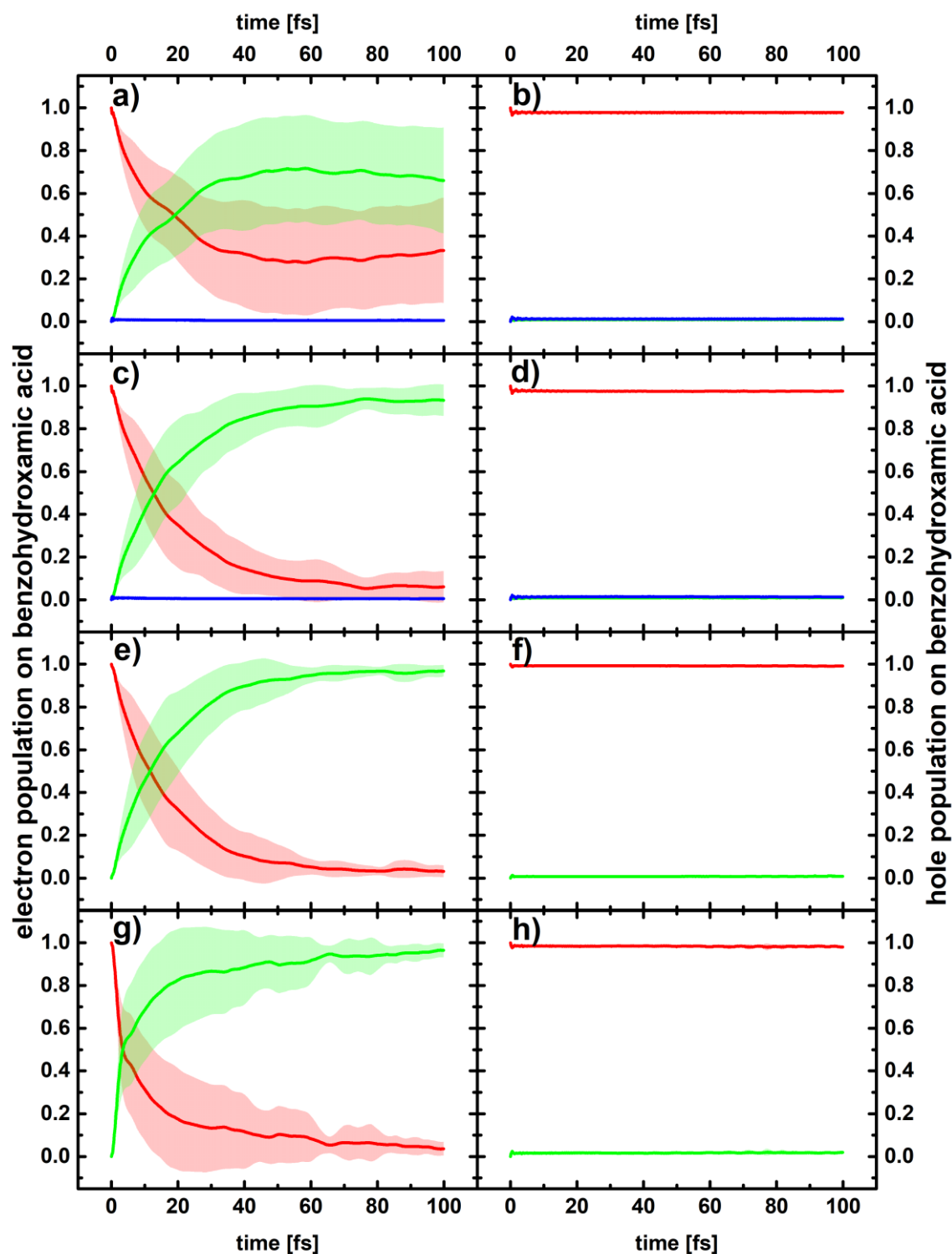


Figure S15. Electron population (left panels) and hole population (right panels) on benzohydroxamic acid (red), TiO_2 (green) and water (blue) averaged over 15 ETDs on **a)/b)** static geometries, **c)/d)** nuclear trajectories with explicit solvation, **e)/f)** nuclear trajectories with explicit water removed, **g)/h)** nuclear trajectories without water. The bold lines denote the mean value, the shaded areas represent the standard deviation centered on the mean value.

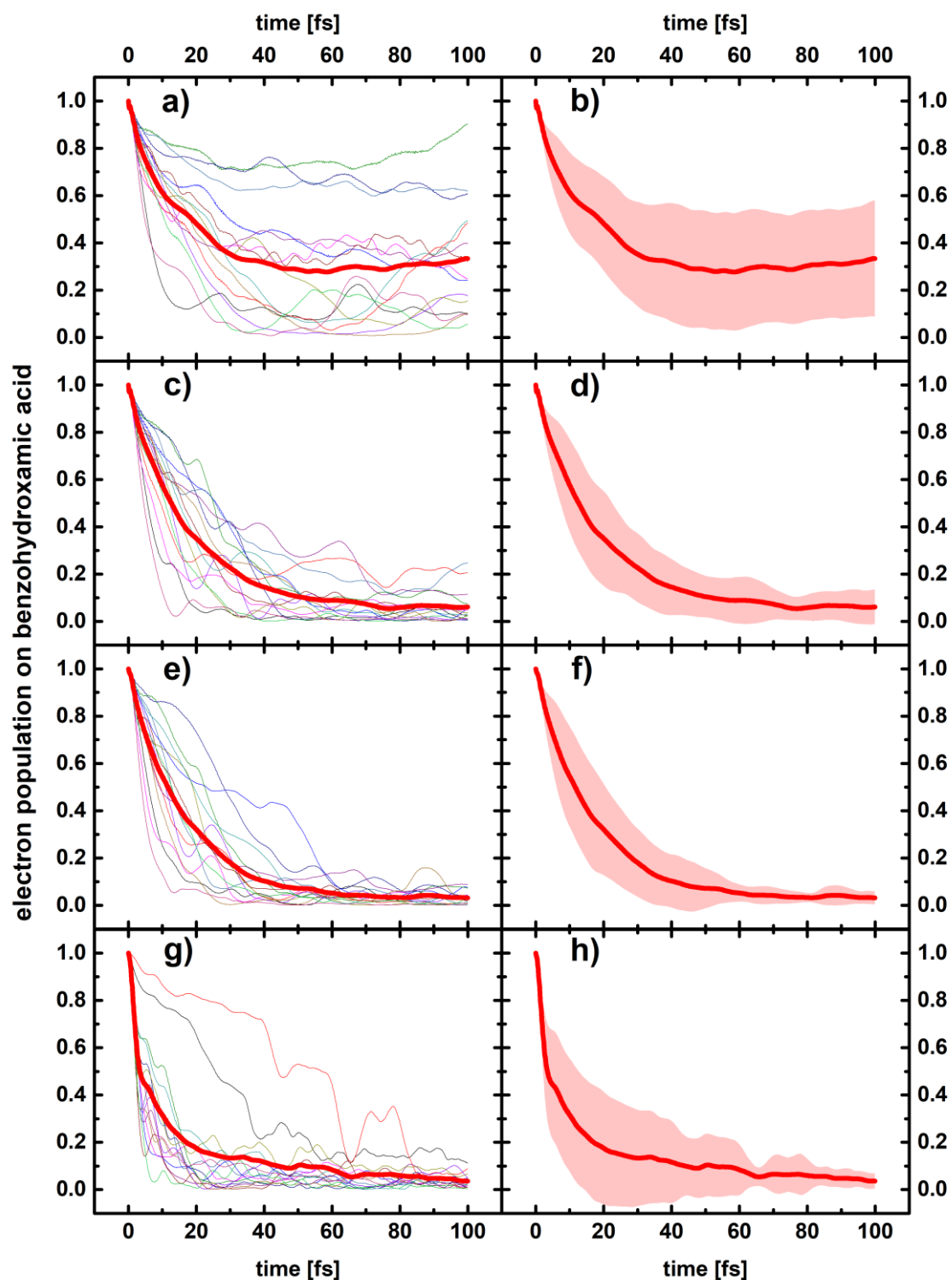


Figure S16. Electron population on benzohydroxamic acid. The left panels show the 15 single ETD runs in narrow lines, the resulting mean average in bold red, the right panels give this same mean average in bold red with the shaded areas representing the standard deviation. Results obtained on **a/b)** static geometries, **c/d)** nuclear trajectories with explicit water, **e/f)** nuclear trajectories with water removed, **g/h)** nuclear trajectories without water.

SI-9 Photoinduced electron injection – Cat-NDI

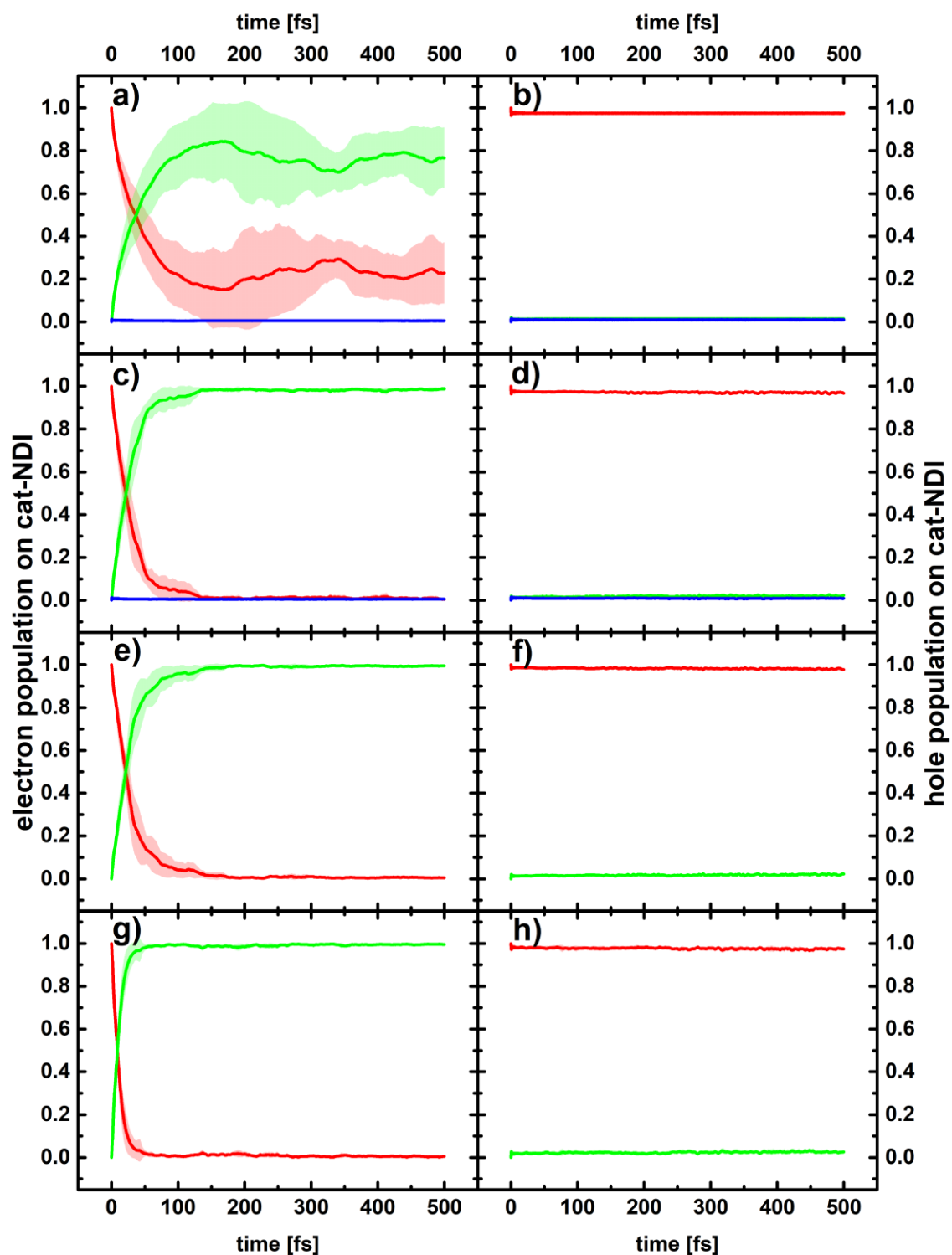


Figure S17. Electron population (left panels) and hole population (right panels) on cat-NDI (red), TiO_2 (green) and water (blue) averaged over 15 ETDs on **a)/b)** static geometries, **c)/d)** nuclear trajectories with explicit solvation, **e)/f)** nuclear trajectories with explicit water removed, **g)/h)** nuclear trajectories without water. The bold lines denote the mean value, the shaded areas represent the standard deviation centered on the mean value.

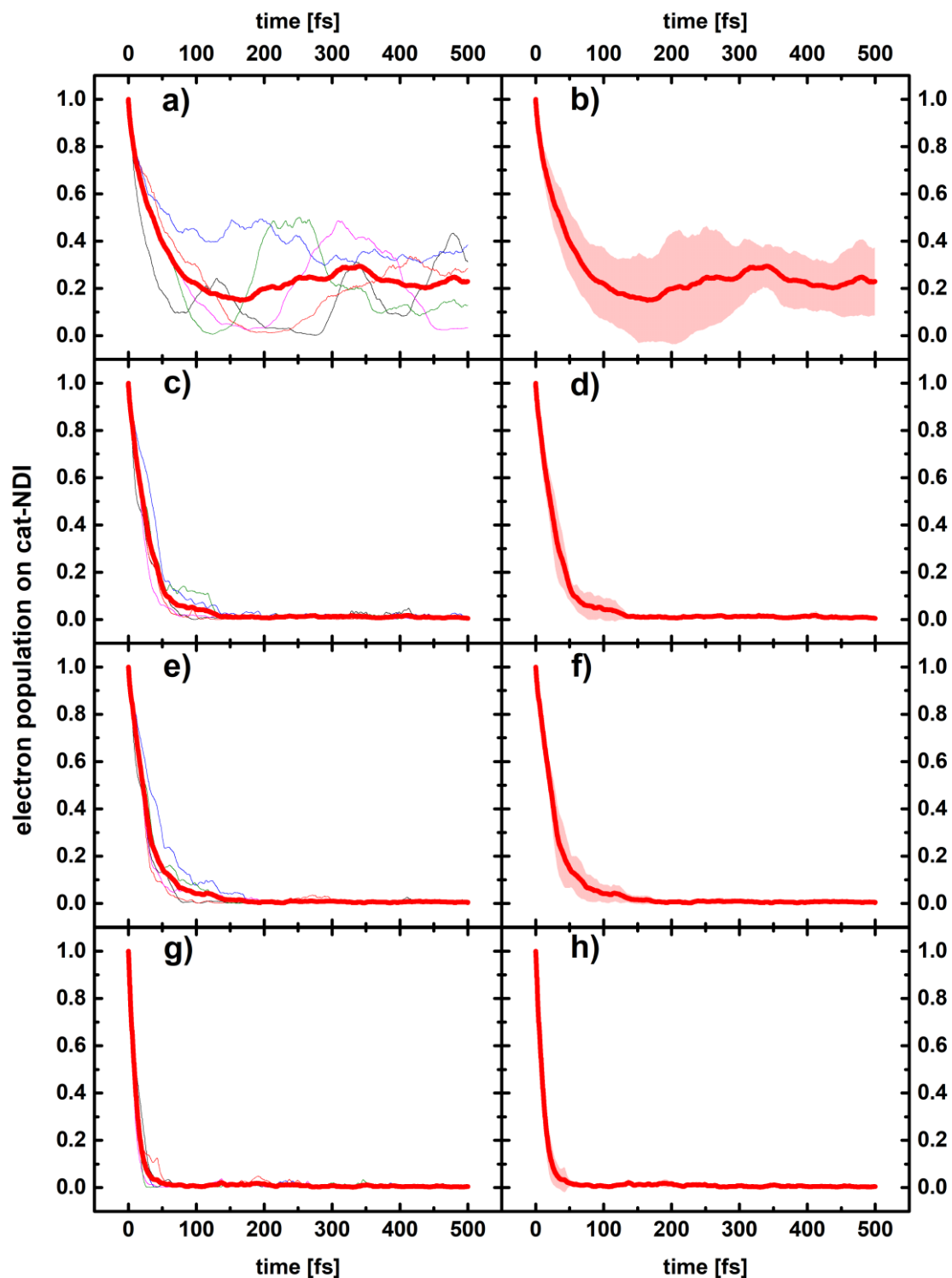


Figure S18. Electron population on cat-NDI. The left panels show the 15 single ETD runs in narrow lines, the resulting mean average in bold red, the right panels give this same mean average in bold red with the shaded areas representing the standard deviation. Results obtained on **a/b)** static geometries, **c/d)** nuclear trajectories with explicit water, **e/f)** nuclear trajectories with water removed, **g/h)** nuclear trajectories without water.

SI-10 Photoinduced electron injection – Ben-NDI

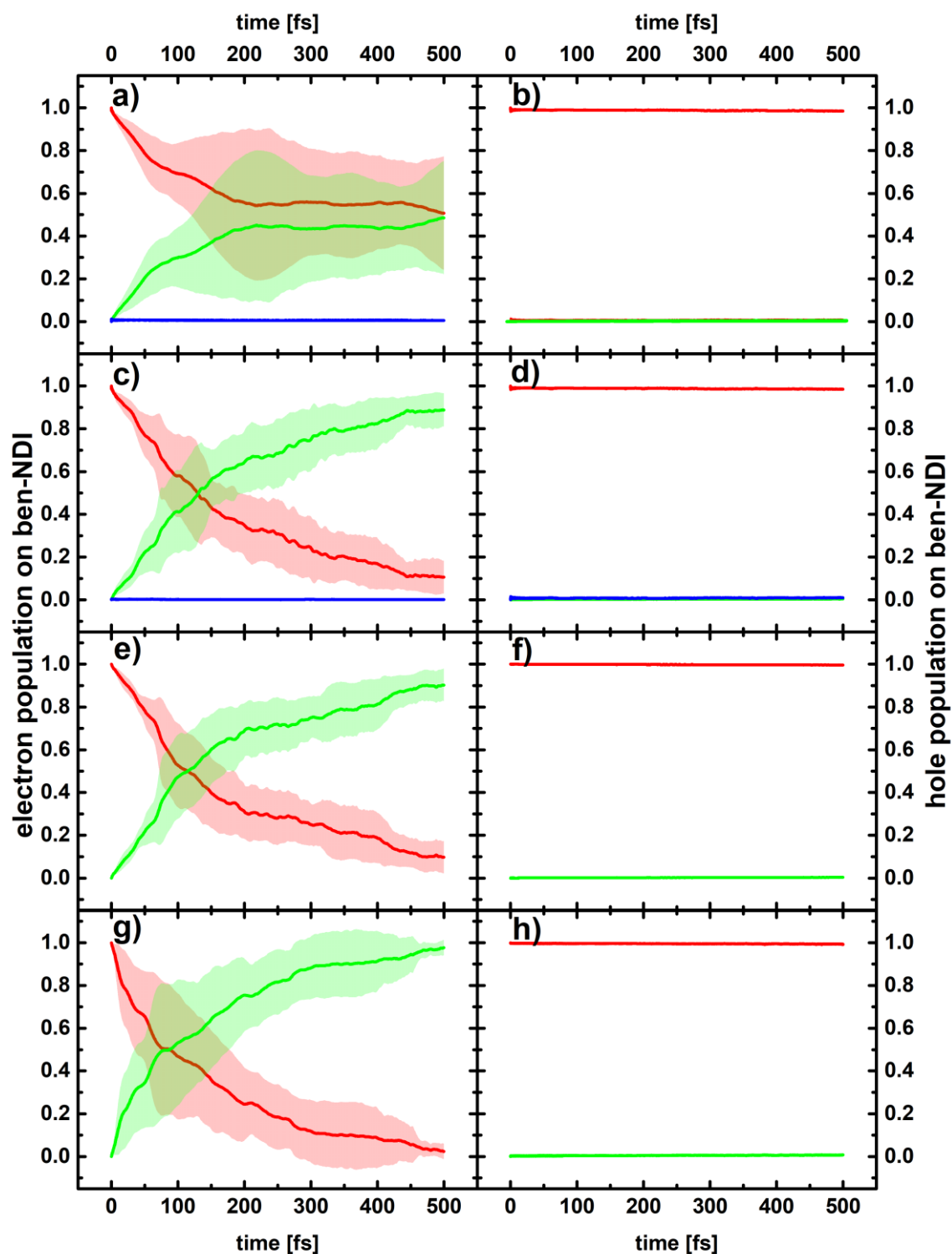


Figure S19. Electron population (left panels) and hole population (right panels) on ben-NDI (red), TiO_2 (green) and water (blue) averaged over 15 ETDs on **a)/b)** static geometries, **c)/d)** nuclear trajectories with explicit solvation, **e)/f)** nuclear trajectories with explicit water removed, **g)/h)** nuclear trajectories without water. The bold lines denote the mean value, the shaded areas represent the standard deviation centered on the mean value.

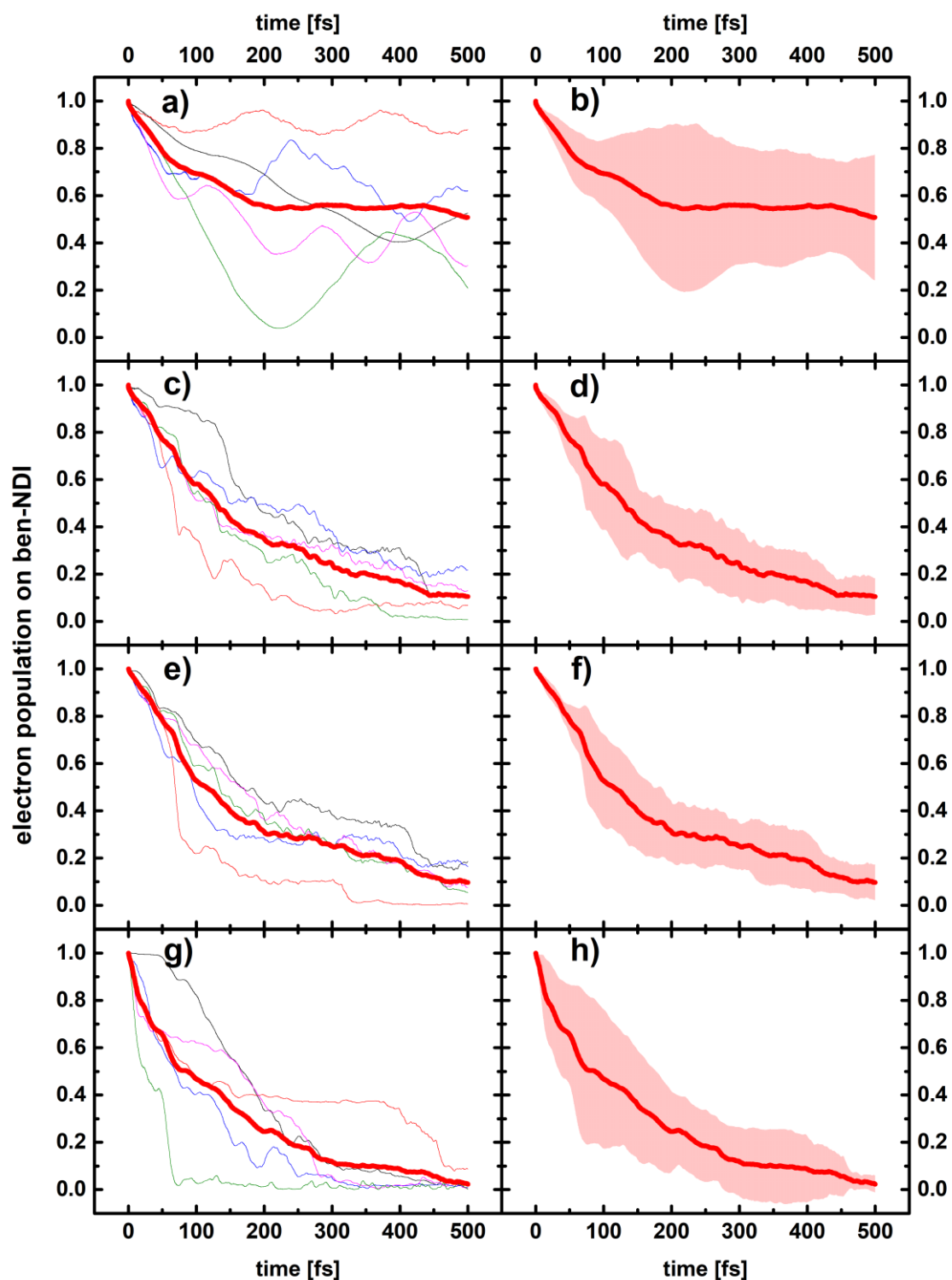


Figure S20. Electron population on ben-NDI. The left panels show the 15 single ETD runs in narrow lines, the resulting mean average in bold red, the right panels give this same mean average in bold red with the shaded areas representing the standard deviation. Results obtained on **a/b**) static geometries, **c/d**) nuclear trajectories with explicit water, **e/f**) nuclear trajectories with water removed, **g/h**) nuclear trajectories without water.

SI-11 Photoinduced electron injection – Hyd-NDI

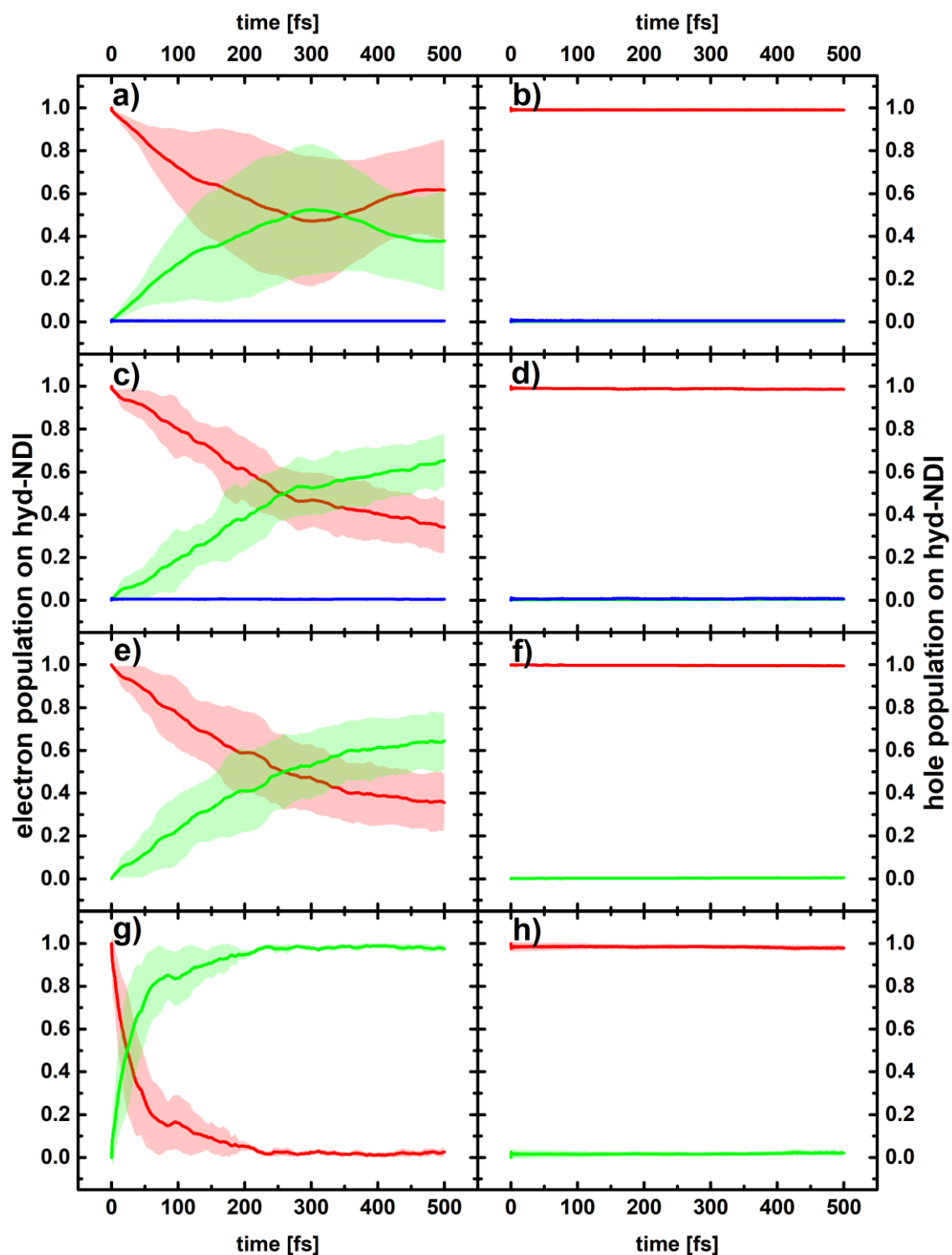


Figure S21. Electron population (left panels) and hole population (right panels) on hyd-NDI (red), TiO_2 (green) and water (blue) averaged over 15 ETDs on **a)/b)** static geometries, **c)/d)** nuclear trajectories with explicit solvation, **e)/f)** nuclear trajectories with explicit water removed, **g)/h)** nuclear trajectories without water. The bold lines denote the mean value, the shaded areas represent the standard deviation centered on the mean value.

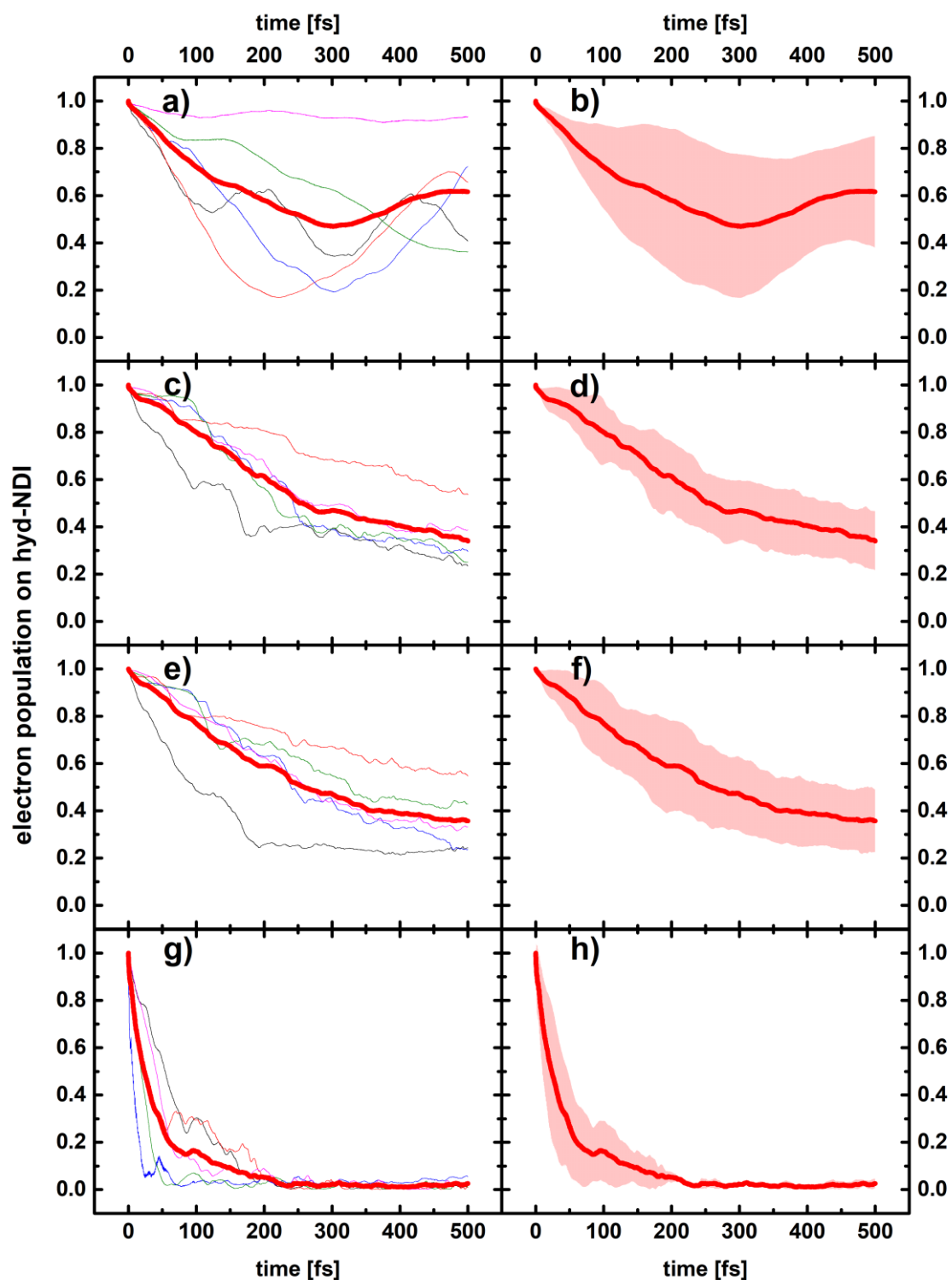


Figure S22. Electron population on hyd-NDI. The left panels show the 15 single ETD runs in narrow lines, the resulting mean average in bold red, the right panels give this same mean average in bold red with the shaded areas representing the standard deviation. Results obtained on **a/b)** static geometries, **c/d)** nuclear trajectories with explicit water, **e/f)** nuclear trajectories with water removed, **g/h)** nuclear trajectories without water.

References

- (1) Elstner, M.; Porezag, D.; Jungnickel, G.; Elsner, J.; Haugk, M.; Frauenheim, Th.; Suhai, S.; Seifert, G. Self-Consistent-Charge Density-Functional Tight-Binding Method for Simulations of Complex Materials Properties. *Phys. Rev. B* **1998**, *58*, 7260–7268.
- (2) Elstner, M.; Frauenheim, T.; Kaxiras, E.; Seifert, G.; Suhai, S. A Self-Consistent Charge Density-Functional Based Tight-Binding Scheme for Large Biomolecules. *physica status solidi (b)* **2000**, *217*, 357–376.
- (3) Frauenheim, T.; Seifert, G.; Elstner, M.; Hajnal, Z.; Jungnickel, G.; Porezag, D.; Suhai, S.; Scholz, R. A Self-Consistent Charge Density-Functional Based Tight-Binding Method for Predictive Materials Simulations in Physics, Chemistry and Biology. *physica status solidi (b)* **2000**, *217*, 41–62.
- (4) Velde, G. te; Bickelhaupt, F. M.; Baerends, E. J.; Fonseca Guerra, C.; van Gisbergen, S. J. A.; Snijders, J. G.; Ziegler, T. Chemistry with ADF. *J. Comput. Chem.* **2001**, *22*, 931–967.
- (5) AMS DFTB 2019.3, SCM, Theoretical Chemistry, Vrije Universiteit, Amsterdam, The Netherlands, <http://www.scm.com>.
- (6) Dolgonos, G.; Aradi, B.; Moreira, N. H.; Frauenheim, T. An Improved Self-Consistent-Charge Density-Functional Tight-Binding (SCC-DFTB) Set of Parameters for Simulation of Bulk and Molecular Systems Involving Titanium. *J. Chem. Theory Comput.* **2010**, *6*, 266–278.
- (7) Berendsen, H. J. C.; Postma, J. P. M.; van Gunsteren, W. F.; DiNola, A.; Haak, J. R. Molecular Dynamics with Coupling to an External Bath. *J. Chem. Phys.* **1984**, *81*, 3684–3690.
- (8) da Silva, R.; Hoff, D. A.; Rego, L. G. C. Coupled Quantum-Classical Method for Long Range Charge Transfer: Relevance of the Nuclear Motion to the Quantum Electron Dynamics. *J. Phys.: Condens. Matter* **2015**, *27*, 134206.
- (9) Monti, A.; Negre, C. F. A.; Batista, V. S.; Rego, L. G. C.; de Groot, H. J. M.; Buda, F. Crucial Role of Nuclear Dynamics for Electron Injection in a Dye–Semiconductor Complex. *J. Phys. Chem. Lett.* **2015**, *6*, 2393–2398.
- (10) Gunnarsson, O.; Lundqvist, B. I. Exchange and Correlation in Atoms, Molecules, and Solids by the Spin-Density-Functional Formalism. *Phys. Rev. B* **1976**, *13*, 4274–4298.
- (11) Jones, R. O.; Gunnarsson, O. The Density Functional Formalism, Its Applications and Prospects. *Rev. Mod. Phys.* **1989**, *61*, 689–746.
- (12) Koopmans, T. Über die Zuordnung von Wellenfunktionen und Eigenwerten zu den Einzelnen Elektronen Eines Atoms. *Physica* **1934**, *1*, 104–113.
- (13) ADF 2019.3, SCM, Theoretical Chemistry, Vrije Universiteit, Amsterdam, The Netherlands, <http://www.scm.com>.
- (14) Becke, A. D. Density-Functional Exchange-Energy Approximation with Correct Asymptotic Behavior. *Phys. Rev. A* **1988**, *38*, 3098–3100.
- (15) Becke, A. D. A New Mixing of Hartree–Fock and Local Density-functional Theories. *J. Chem. Phys.* **1993**, *98*, 1372–1377.
- (16) Lee, C.; Yang, W.; Parr, R. G. Development of the Colle-Salvetti Correlation-Energy Formula into a Functional of the Electron Density. *Phys. Rev. B* **1988**, *37*, 785–789.
- (17) Van Lenthe, E.; Baerends, E. J. Optimized Slater-Type Basis Sets for the Elements 1–118. *Journal of Computational Chemistry* **2003**, *24*, 1142–1156.
- (18) Grimme, S.; Antony, J.; Ehrlich, S.; Krieg, H. A Consistent and Accurate Ab Initio Parametrization of Density Functional Dispersion Correction (DFT-D) for the 94 Elements H–Pu. *J. Chem. Phys.* **2010**, *132*, 154104.
- (19) Grimme, S.; Ehrlich, S.; Goerigk, L. Effect of the Damping Function in Dispersion Corrected Density Functional Theory. *Journal of Computational Chemistry* **2011**, *32*, 1456–1465.
- (20) Pye, C. C.; Ziegler, T. An Implementation of the Conductor-like Screening Model of Solvation within the Amsterdam Density Functional Package. *Theor Chem Acc* **1999**, *101*, 396–408.
- (21) Ooyama, Y.; Yamaji, K.; Ohshita, J. Photovoltaic Performances of Type-II Dye-Sensitized Solar Cells Based on Catechol Dye Sensitizers: Retardation of Back-Electron Transfer by PET (Photo-Induced Electron Transfer). *Mater. Chem. Front.* **2017**, *1*, 2243–2255.
- (22) Sakai, N.; Mareda, J.; Vauthey, E.; Matile, S. Core-Substituted Naphthalenediimides. *Chem. Commun.* **2010**, *46*, 4225–4237.

- (23) Narsaria, A. K.; Ruijter, J. D.; Hamlin, T. A.; Ehlers, A. W.; Guerra, C. F.; Lammertsma, K.; Bickelhaupt, F. M. Performance of TDDFT Vertical Excitation Energies of Core-Substituted Naphthalene Diimides. *Journal of Computational Chemistry* **2020**, *41*, 1448–1455.
- (24) Glorius, M.; Moll, H.; Bernhard, G. Complexation of Uranium(VI) with Aromatic Acids in Aqueous Solution – a Comparison of Hydroxamic Acids and Benzoic Acid. *Radiochimica Acta* **2007**, *95*, 151–157.
- (25) Fujisawa, J.; Eda, T.; Hanaya, M. Comparative Study of Conduction-Band and Valence-Band Edges of TiO₂, SrTiO₃, and BaTiO₃ by Ionization Potential Measurements. *Chemical Physics Letters* **2017**, *685*, 23–26.
- (26) Menzel, J. P.; de Groot, H. J. M.; Buda, F. Photoinduced Electron Transfer in Donor–Acceptor Complexes: Isotope Effect and Dynamic Symmetry Breaking. *J. Phys. Chem. Lett.* **2019**, *10*, 6504–6511.